

# FORMULATION AND TESTING OF A PROGRAM FOR THE OBJECTIVE ASSEMBLY OF METEOROLOGICAL SATELLITE CLOUD OBSERVATIONS<sup>1</sup>

ROLAND E. NAGLE, JAMES R. CLARK, MANFRED M. HOLL, and CHRISTOPHER A. RIEGEL<sup>2</sup>

Meteorology International Inc., Monterey, Calif.

## ABSTRACT

The formulation and testing of an assembly program, which is designed to assimilate information derived from satellite videographs and produce a probability-of-cloudiness analysis for times concurrent with standard, synoptic, upper-air observations, is described. The program is based on the fact that layer-cloudiness distributions (in the synoptic range of scale) can be adequately depicted by specification of the net horizontal and vertical displacement of an array of parcels on a suitable isentropic surface. The results show that the accuracy of the probability-of-cloudiness analyses depends more on the accuracy of the diagnosed net lifting or subsidence of the parcels than on either the initial moisture distribution or the constants contained in the formulation of the program. The potential advantages of this program as an operational tool are discussed.

## 1. INTRODUCTION

The pre-emptive function of an Environmental Analysis and Prediction System is to assemble all pertinent information into an accurate representation of the current state of the ocean-atmosphere complex. For the atmosphere, this representation may be in terms of the spatial distribution of the mass structure,<sup>3</sup> the motion field, the hydrometeors, and the heat sources and sinks. Current operational numerical weather analysis systems produce analyses primarily in terms of the distributions of the mass structure and the motion field; they are not designed to accommodate observations of the hydrometeors or observations relating to the heat sources or sinks. The current distribution of the hydrometeors is, however, operationally important, and their delineation from the numerically produced analyses depends on subjective interpretations based on empirical rules and accumulated past experience. Therefore, objective analyses of the current distribution of the hydrometeors would be operationally useful and would complement the existing numerically produced fields.

Satellite videograph observations provide data on the cloud distributions; however, the information arrives in successive swaths which are not normally coincident with the conventional synoptic observations. To produce a synoptic cloud analysis based on satellite data, the information in each of the successive swaths must be rationally

brought forward to the time of the latest conventional observations. In order to accomplish this, the manner in which cloud patterns are generated needs to be known. Clouds, of course, are the resultant of lifting and, in the synoptic range of scale, the net lifting of an air parcel can be approximated by determining the change in pressure which the parcel experienced along its isentropic trajectory. In following the motion of a parcel on an isentropic surface, it is assumed that the potential temperature is conservative; in the real atmosphere this condition is not strictly fulfilled because of non-adiabatic processes. When condensation occurs, for example, the potential temperature of the parcel is increased by the release of latent heat and the parcel moves away from its original isentropic surface. The effects of radiational heating and cooling, evaporation, and convective activity can also lead to discrepancies between actual trajectories and those computed under dry adiabatic assumptions. However, in our previous work on the interpretation of cloud evolutions [1], it was found that the major portion of layer-cloudiness distributions can be accounted for by the time-integrated horizontal and vertical dry adiabatic displacement of parcels on a suitable isentropic surface. Therefore, from a diagnosis (i.e., a determination of derivable parameters from available parameters) of the displacement of an array of parcels on the isentropic surface, the inherent information in each of the successive satellite swaths may be brought forward along the time axis. The vehicle to accomplish this is the Diagnostic-Cycle Routine, the formulation and testing of which has been documented elsewhere [2]. This paper details the modification and testing of the routine for use as a cloud assembly program.

<sup>1</sup> The studies reported here were sponsored by Project FAMOS, U.S. Fleet Weather Central under Contract No. N62306-1775.

<sup>2</sup> Present affiliation, San Jose State College, San Jose, Calif.

<sup>3</sup> By virtue of the hydrostatic equation and the gas law, the three-dimensional distribution of air density also prescribes the distribution of pressure, virtual temperature, corresponding lapse rates, etc. All these distributions are collectively referred to as the "mass" structure of the atmosphere.

## 2. SUMMARY OF OPERATIONS PERFORMED BY THE CLOUD ASSEMBLY PROGRAMS

All operations performed by the Cloud Assembly Program are for fields on a selected isentropic surface as depicted in a  $126 \times 126$  gridpoint array for the Northern Hemisphere. The computations in this study were for the  $305^\circ$  K. potential temperature surface; however, the program is general and can be performed on any isentropic surface existing between the surface and the 200-mb. level.

The fields required are: (1) an estimate of the moisture distribution (in terms of mixing ratio) at the initial cycle time of the integration, (2) the hourly pressure-height fields for the selected isentropic surfaces, (3) the diagnosed winds at hourly time steps for each 12-hr. period of integration, and (4) the satellite cloud observations prepared in digital form.

The estimate of the initial moisture distribution was obtained in the following manner: Because of the particular mass-structure model [3] used by the U.S. Fleet Numerical Weather Facility (FNWF), it is possible to diagnose (in a  $63 \times 63$  gridpoint array for the Northern Hemisphere) the Montgomery stream function and the pressure-height of any potential temperature surface within the limits of the atmosphere encompassed by the model. Specification of the pressure-height distribution of an isentropic surface is equivalent to defining the temperature distribution. Knowing the pressure and temperature of a parcel (gridpoint) defines the parcel's saturation mixing ratio value and this parameter was calculated using standard sub-routines for transcendental functions; this field was expanded by a double quadratic interpolation to a  $126 \times 126$  gridpoint array. The initial moisture distribution used for the first cycle of integration was a percentage of the saturation mixing ratio of each parcel.

The hourly pressure-height fields for the isentropic surface are available as a product of one of the sub-routines of the Diagnostic-Cycle Routine. From the hourly interpolated distributions of the isentropic parameters, it is possible to diagnose corresponding horizontal velocity distributions for the isentropic surface. The Cloud Assembly Program linearly interpolates both the pressure-height fields and the wind fields to half-hourly values. By means of these winds, each parcel in the field is displaced along the interpolated evolution of the isentropic surface. This displacement is accomplished in terms of an *equivalent* mixing ratio which incorporates the moisture in both vapor and liquid form.

The displaced parcels arrive at a new location and at a new pressure-height at the end of each time-step. Following this operation, weak lateral smoothing is performed on the brought-forward mixing ratio field. At the appropriate times, the satellite cloud data (prepared in digital format) are introduced into the Program. Joint comparisons are then made, at each gridpoint within the region defined by the satellite videograph coverage, between the presence or absence of clouds, the parcel mixing ratio, and a pressure-dependent, critical mixing ratio

value for the presence of cloudiness. Where contradictions are found, the mixing ratio of the parcel is adjusted to one side or the other of the critical value depending on the form of the contradiction. The adjusted mixing ratio at each point in the field and at each time-step is then compared with a pressure-dependent, maximum-allowable moisture content for the parcel. If the mixing ratio exceeds the maximum allowable value for the parcel's pressure-height, the excess is removed and stored in an analogy to precipitation. The integration proceeds in this manner for a 12-hr. period. At the end of a 12-hr. cycle, the mixing ratio is converted into a probability-of-significant-cloudiness parameter based again on a pressure-dependent function. The final outputs are linedrawn charts for the Northern Hemisphere which show the geographic distribution of: the probability of significant cloudiness for the time that is coincident with the latest synoptic observations and the accumulated precipitation for the 12-hr. period of integration.

## 3. FORMULATION OF THE PROGRAM THE GOVERNING EQUATION

We are concerned with the distribution of properties of an atmospheric layer which is defined by isentropic surfaces. Let  $M_w$ ,  $M_l$ , and  $M_d$  represent the respective masses of water vapor, liquid water, and dry air in the layer per unit area. By definition, the total mass of the moist air and liquid water is

$$S^* \equiv M_w + M_l + M_d. \quad (1)$$

We define the "equivalent" mixing ratio as

$$W^* \equiv (M_w + M_l) / M_d. \quad (2)$$

Under adiabatic conditions, the relevant mass-continuity equations for the above parameters are:

$$\partial M_w / \partial t = -\nabla_\theta \cdot [M_w \mathbf{V}_H] + \dot{M}_w \quad (3)$$

$$\partial M_l / \partial t = -\nabla_\theta \cdot [M_l \mathbf{V}_H] + \dot{M}_l \quad (4)$$

$$\partial M_d / \partial t = -\nabla_\theta \cdot [M_d \mathbf{V}_H] + \dot{M}_d \quad (5)$$

$$\partial S^* / \partial t = -\nabla_\theta \cdot [S^* \mathbf{V}_H] + \dot{S}^* \quad (6)$$

where the terms involving the superscript "dot" represent the generation or deletion of mass from the parcel.

In treating saturation and condensation processes, the parameter  $W^*$  is of greater physical significance than the sum of parameters  $M_w$  and  $M_l$ . It is germane therefore, to select  $W^*$  as the principal dependent variable for defining the water-mass distribution. Adding equations (3) and (4), substituting from equation (2) for  $(M_w + M_l)$ , and subtracting equation (5) multiplied by  $W^*$  from the resulting equation yield

$$\partial W^* / \partial t = -\mathbf{V}_H \cdot \nabla_\theta W^* + \dot{W}^*. \quad (7)$$

The term  $\dot{W}^*$  includes mixing and precipitation processes.

Equation (7), modified with a lateral diffusion coefficient, is used as the pertinent governing equation, thus

$$\partial W^*/\partial t = -V_H \cdot \nabla_H W^* + \mu \nabla_H^2 W^* + \dot{W}^*. \quad (8)$$

The continuity equation for mixing ratio expressed only in terms of the mass of vapor and dry air is identical in form to equation (8). With the understanding that we are treating the combined mass of water in both vapor and liquid form, the asterisk and the term "equivalent" will henceforth be deleted.

#### OPERATIONS PERFORMED ON THE MIXING RATIO FIELD

Under advection, the mixing ratio is parcel-conservative except for the addition and removal of water substance. Since the parcel is defined by the potential temperature, the pressure variation also defines the temperature variation. In this context, the only independent variable of state is the pressure.

Each parcel in the layer migrates horizontally and vertically in its isentropic trajectory. At any instant, the mixing ratio of a parcel is permitted to range from dry,  $W=0$ , to a value associated with the beginning of cloudiness,  $W_i$ , and up to a maximum value,  $W_m$ . In the interval  $W_i < W < W_m$ , the mixing ratio includes cloud droplets as well as vapor. The maximum mixing ratio,  $W_m$ , is attained when the air is completely saturated with respect to vapor and fully cloudy. The present program requires the specification of  $W_i$  and  $W_m$  as a function of pressure; the derivation of these functional relationships is provided in the Appendix.

For a parcel at pressure,  $p$ , with a mixing ratio  $W > W_i$ , the proportion of its volume,  $\delta$ , which is filled by cloud is also required. This is estimated by

$$\delta = \frac{W - W_i}{W_m - W_i}. \quad (9)$$

The denominator,  $W_m - W_i$ , represents the dynamic range of the mixing ratio as an indicator of layer-cloud amount. The critical value of  $\delta$  for demarcating significant cloudiness undoubtedly does vary, but for the purposes of this study it has been assumed to be  $\delta_c = 0.3$ ; i.e., three-tenths of the volume is cloud filled.

The input of information from cloud observations is accomplished by enforcing compatibility of the mixing ratio. For those times and gridpoints at which there are cloud observations from the satellite, the compatibility is enforced as follows: For a yes-cloudiness reading, the compatibility is in order if  $\delta \geq \delta_c$ . If  $\delta < \delta_c$ , the value of  $W$  is stepped up to

$$W = W_i + \alpha[W_m - W_i], \quad (10)$$

giving a value  $\delta = \alpha$ . For a no-cloudiness reading, the compatibility is in order if  $\delta \leq \delta_c$ . If  $\delta > \delta_c$ , the value of  $W$  is reduced to

$$W = W_i + \beta[W_m - W_i], \quad (11)$$

giving a value  $\delta = \beta$ . Both  $\alpha$  and  $\beta$  may be varied in the Program.

The precipitation field is accumulated as follows: At each time step, a test is made to assure that  $W \leq W_m$  everywhere. This again requires a table look-up procedure for  $W_m$ . At those gridpoints where advection and lifting have resulted in  $W > W_m$ , the excess  $W_p = W - W_m$  is removed and the moisture is added to the precipitation-accumulator field. The amount of precipitation added at that gridpoint to the accumulator field is proportional to  $R$ , where

$$R = W_p \rho \quad (12)$$

and  $\rho$  is the dry-air density of the parcel from which the moisture is removed. This density is also obtained by table look-up routine with pressure as entry.

The accumulated precipitation field was produced as part of the output of each numerical experiment; no attempt was made to verify the accuracy of the resulting fields as it was a by-product of the primary objective of this study. Therefore, only one example of this field is shown in this paper to illustrate the nature of the product.

The output of the cloudiness analysis is accomplished by transforming  $W$  into the field of  $\delta$  as expressed by equation (9). The positive values of  $\delta$  may be interpreted as the proportion of the volume filled by cloud; we selected the value  $\delta = 0.6$  (about seven-tenths cloud cover) as demarcating areas of broken, significant cloudiness. Values of  $W$  less than  $W_i$  transform into negative  $\delta$ ; the larger the value of  $\delta$  in a negative sense, the greater is the degree of dryness. This output may be taken at selected intervals in time.

#### 4. PREPARATION OF THE SATELLITE CLOUD DATA

In order to test the Cloud Assembly Program, it was necessary to prepare the satellite data in digital form. Videographs of the cloud patterns obtained from the TIROS IX satellite were used as the basic data. A sector of the  $126 \times 126$  Northern Hemisphere grid based on the videograph coverage obtained on a particular orbit was first defined; this sector was centered on the approximate longitude of the orbital sub-satellite track and its width was  $40^\circ$  of longitude. It extended from the equator to the most northerly latitude of the usable videograph coverage.

The cloud patterns for the sector were then analyzed using gridded prints of the original videographs. The interpretation of the cloud patterns was comparable to that used in preparing the operational nephanalyses; attention was focused on organized cloud patterns of 80 percent or greater coverage. Areas of less than 80 percent coverage were included in the nephanalyses when they were integral components of organized cloud systems. It was attempted to exclude from the nephanalyses clouds attributable to local conditions, i.e., coastal stratus,

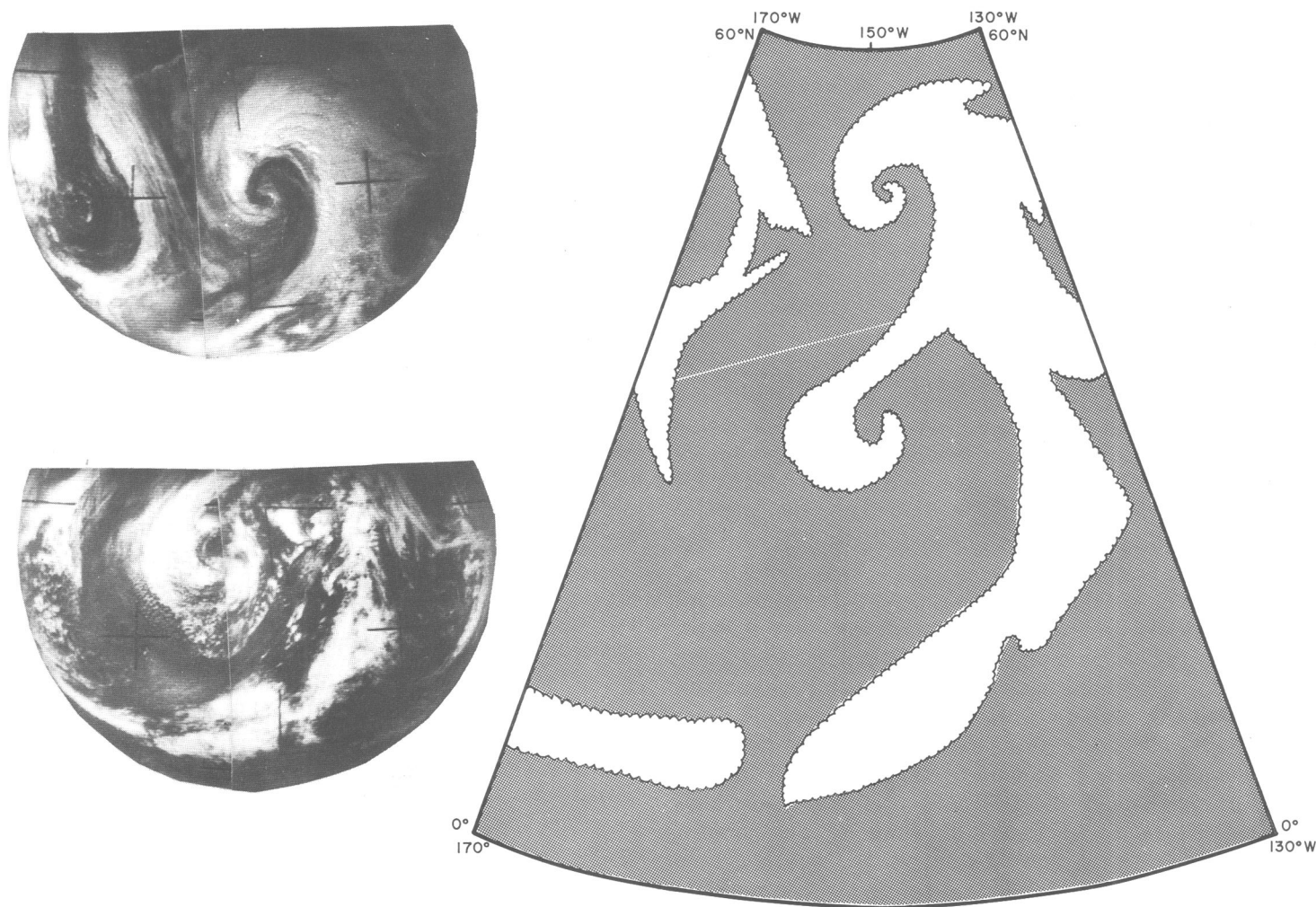


FIGURE 1.—Example of nephanalysis depiction of cloud patterns viewed in the original videographs.

orographic clouds, diurnal cumulus clouds, etc., and small-scale convective clouds (even if they existed over large areas). An example of a nephanalysis prepared in this manner is shown in figure 1. Two picture doublets from TIROS IX pass 0129 are shown on the left of this figure; the corresponding nephanalysis for the sector is shown on the right. Shaded areas represent the *absence* of significant cloudiness.

The next step was to convert the nephanalysis to digital form; this was accomplished by manually reading the "cloud"—"no-cloud" information at gridpoints and converting these data to punched cards. All passes of TIROS IX covering the test period from 0000 GMT, February 1 through 0000 GMT, February 3, 1965, were prepared in this manner and were available as input data for the Cloud Assembly Program.

## 5. RESULTS

The Cloud Assembly Program was tested by running it for the 48-hr. period 0000 GMT, February 1 through 0000 GMT, February 3, 1965. Several variations were tried to ascertain the significance of the various constants

prescribed in the formulation. The results of these tests are now presented.

### EXPERIMENT NO. 1

The first test of the Program was made with the constants of equations (10), (11), and (8) set at the following values:  $\alpha=0.6$ ,  $\beta=0.1$ , and  $\mu=1/32$ . The diagnosed wind fields used in this integration were based on the geostrophic approximation modified to accommodate the inferred field of momentum convergence for the layer [2]. The initial moisture distribution used was 90 percent of the saturation mixing ratio obtained from the conversion of the pressure-height distribution of the 305° K. potential temperature surface; this analysis is shown in figure 2. In accordance with column (13) of table A1, a mixing ratio distribution of 90 percent of saturation with respect to vapor constitutes a totally cloudy initial state for the atmosphere. While this is an unrealistically moist atmosphere, the initial mixing ratio field is used only once, e.g., when the advected moisture field is compared with the satellite cloud observations obtained during the first 24 hr. of integration. Thus,



after the first 24 hr., the mixing ratio field will have been adjusted in accordance with the actual cloud patterns and the resulting moisture distribution should then be compatible with the actual large-scale atmospheric moisture distribution.

A composite nephanalysis of the cloud information which was assimilated into the Program during the first 24-hr. period of integration is shown in figure 3. The probability-of-cloudiness analysis resulting from the first 12-hr. integration (1200 GMT, February 1) is shown in figure 4. The effect of the initial moisture distribution is immediately apparent in this latter figure. The regions where the moisture field was *not* modified on the basis of the cloud information shows a higher probability of cloudiness than those regions where the moisture distribution was modified on the basis of the cloud information. It was expected that this would be the case and that the Program would have to be cycled through at least one 24-hr. period before the moisture field would be properly adjusted.

The probability-of-cloudiness analysis resulting from the second 12-hr. period of integration is shown in figure 5 and the corresponding accumulated precipitation distribution is shown in figure 6. It can be noted that the pattern of the probability-of-cloudiness analysis shown in figure 5 becomes progressively smoother proceeding in a counterclockwise sense from 170° W. The latest cloud information was assimilated into the Program in the sector between 130° W. and 170° W. longitude at approximately 2330 GMT, February 1; thus, the moisture field in this sector had undergone the most current modification on the basis of the cloudiness and was not modified by advection or smoothing. Proceeding counterclockwise, we see that the moisture field had undergone progressively more modification by the advection of the parcels on the isentropic surface and, among other things, by lateral smoothing. By comparing the probability-of-cloudiness analysis for 0000 GMT, February 2 in the western Pacific Ocean region with the cloud information from this same area (pass 0120) which was assimilated into the Program at 0330 GMT, February 1, it can be seen that very little of the information in the cloud swath has been retained at the end of the 24-hr. integration.

#### EXPERIMENT NO. 2

In an attempt to retain more of the character of the cloudiness patterns in the probability-of-cloudiness analysis, the Program was re-run for the same period with different values for the constants of equations (10), (11), and (8). In this test the following values were used:  $\alpha=0.8$ ,  $\beta=-0.1$ , and  $\mu=1/512$ . These values represent a rather drastic change from the previous experiment. The initial moisture field, the winds, and the cloudiness analyses were identical to those used in Experiment No. 1.

The resulting probability-of-cloudiness analyses and the corresponding accumulated precipitation distribution (not shown) were practically identical with those produced in Experiment No. 1. The gradients between high and low

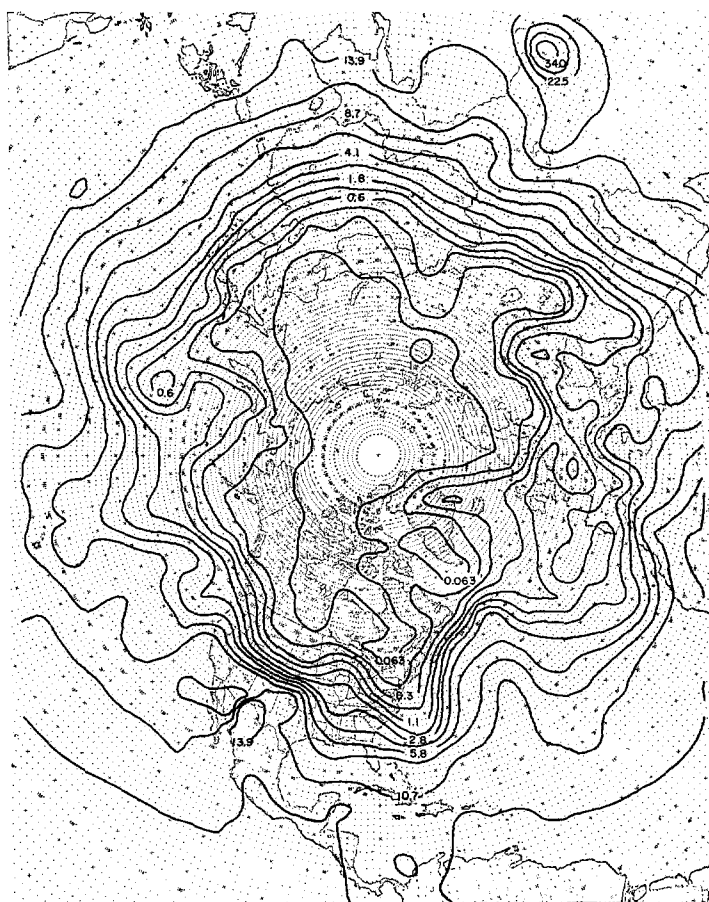






FIGURE 3.—Composite nephalanalysis of satellite cloud information for the period 0000 GMT, February 1 to 0000 GMT, February 2, 1965.



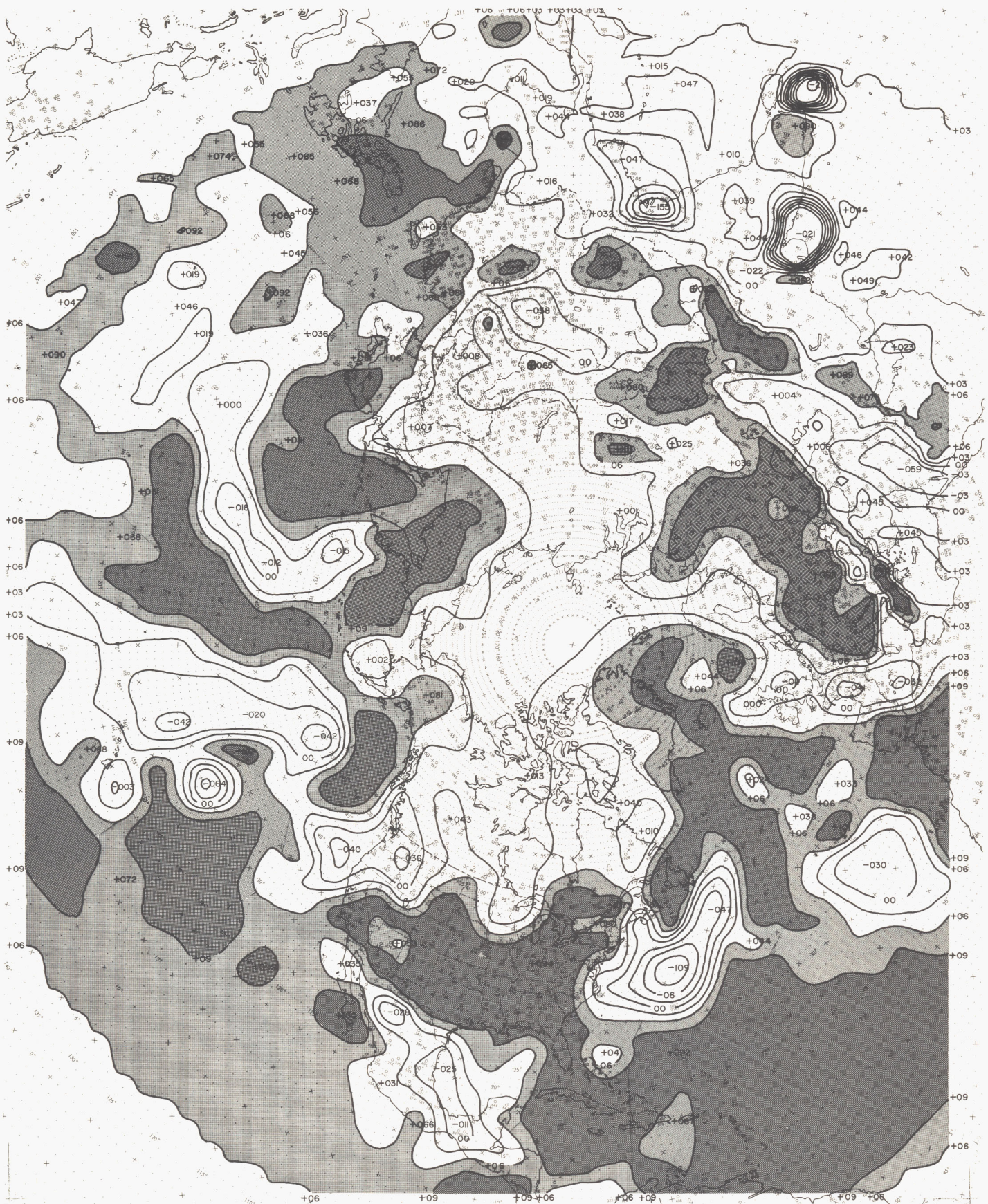


FIGURE 4.—Experiment No. 1: probability-of-cloudiness analysis, 1200 GMT, February 1, 1965. Contours are isolines of  $\delta$  (for explanation see section 3). Light shading indicates seven- to nine-tenths cloud cover. Heavy shadings indicate greater than nine-tenths cloud cover.







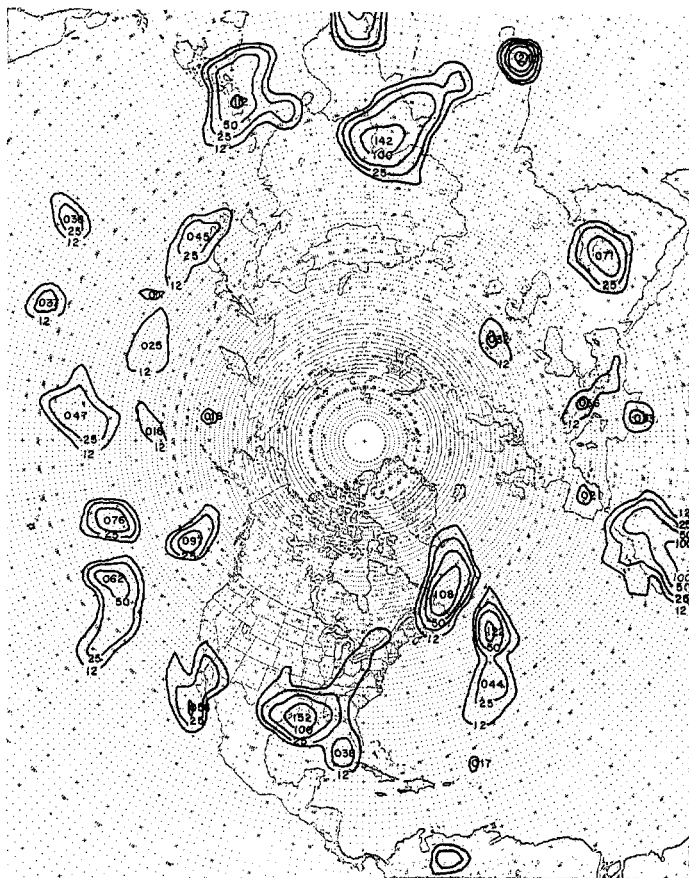


FIGURE 6.—Experiment No. 1: accumulated precipitation for the period 1200 GMT, February 1 to 0000 GMT, February 2, 1965 (mm.  $\times 10^{-1}$  per 3 km. depth of the atmosphere). Last digit omitted from the contour line labels.

strophic wind and they can be diagnosed with relative efficiency. For the period 0000 GMT, February 2 through 0000 GMT, February 3, 1965, the balance equation wind was used for the integrations in the Cloud Assembly Program. The balance equation for the isentropic surface was solved in the manner described by 'Arnason [5]. The details of the computation have been reported on by 'Arnason and Reese [6].

The initial moisture distribution used in this experiment was the mixing ratio field for 0000 GMT, February 2, 1965 which resulted from the integration carried out in Experiment No. 2. The composite nephanalysis of the cloud information assimilated into the Program during this 24-hr. test period is shown in figure 7. The resulting probability-of-cloudiness analysis for 1200 GMT, February 2 is shown in figure 8. The probability-of-cloudiness analysis for the second 12-hr. period of integration of the experiment is shown in figure 9.

A comparison of these results with the results of Experiment No. 1 shows that the resultant distributions obtained from the balance equation wind are equally as reasonable as those obtained with use of the winds modified



FIGURE 7.—Composite nephanalysis of satellite cloud information for the period 0000 GMT, February 2 to 0000 GMT, February 3, 1965.

in accordance with the inferred field of momentum convergence. This is achieved with a 50 percent reduction in the computation time, viz., 21 min. versus 42 min. per 12-hr. integration.

## EXPERIMENT NO. 4

This experiment was in the nature of a verification of the Cloud Assembly Program. The Program was cycled for a 12-hr. period *without* cloud information having been assimilated into the system. The period chosen for this experiment was from 1200 GMT, February 2 through 0000 GMT, February 3, 1965. The initial moisture distribution used was the resultant mixing-ratio field for 1200 GMT, February 2. The balance equation winds were used in the integrations. Probability-of-cloudiness analyses were produced at the end of each 3-hr. interval during the period. Although the integration started with the moisture distribution for 1200 GMT, February 2, the resulting fields are 24-hr. (approximately) integrations from the time of the last modification of the moisture field. For example, the last modification made (on the



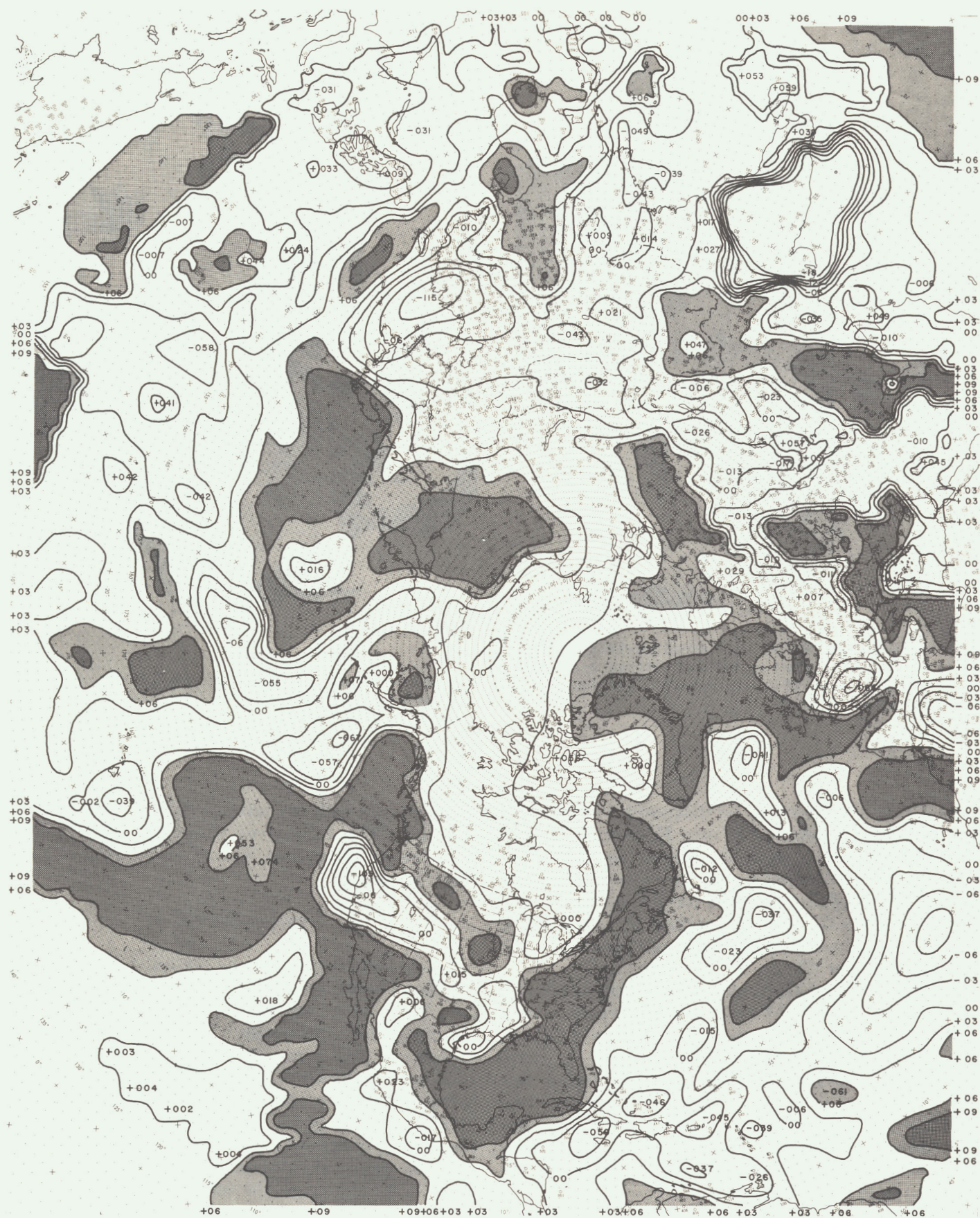
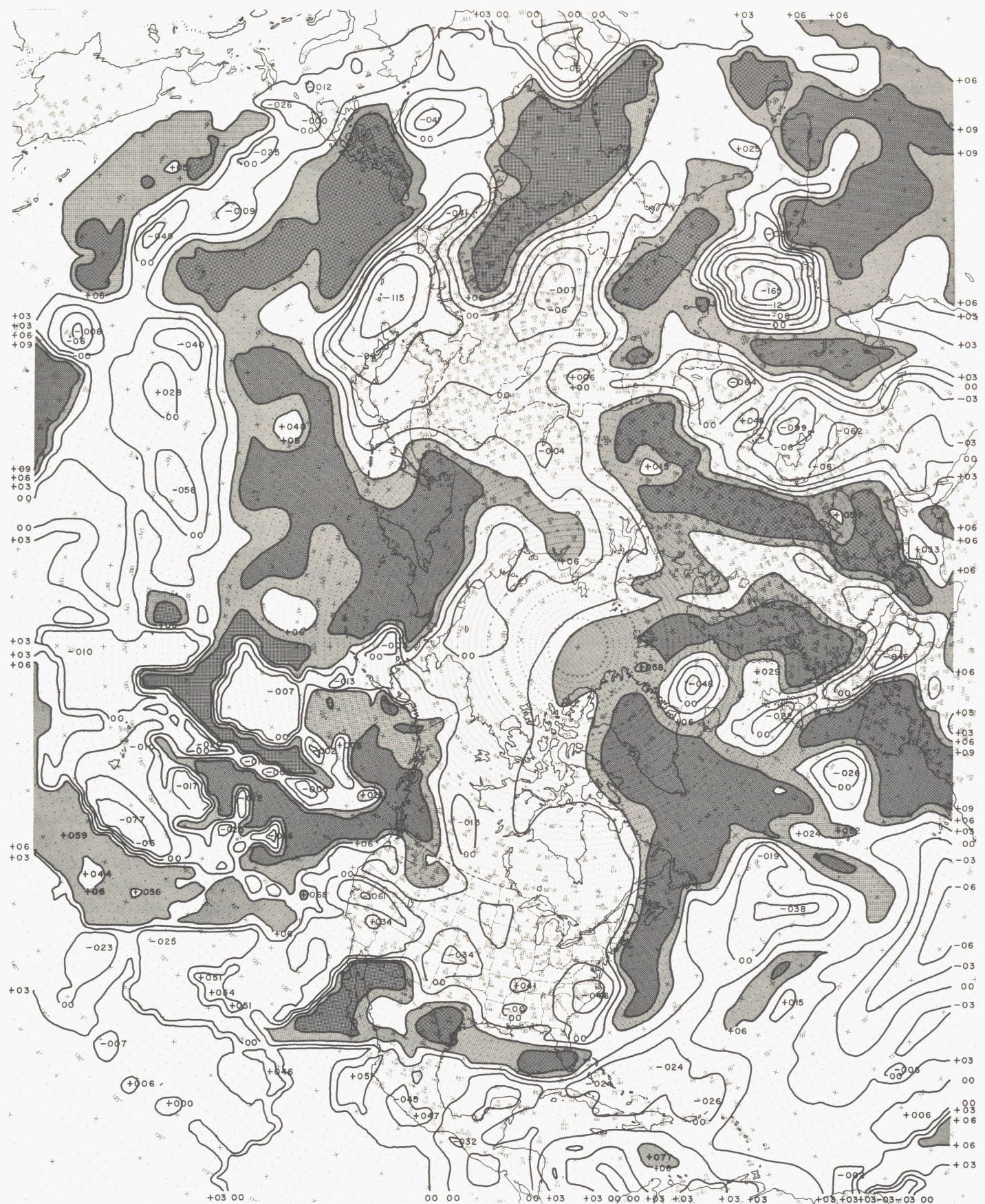


FIGURE 8.—Experiment No. 3: probability-of-cloudiness analysis, 1200 GMT, February 2, 1965. (For legend see fig. 4.)







basis of the cloud information) on the moisture content of the parcels arriving in the sector between  $10^{\circ}$  and  $50^{\circ}$  W. longitude in figure 10 at 1500 GMT, February 2 was at approximately 1530 GMT, February 1.

Comparisons were made between the probability-of-cloudiness analyses produced by the Cloud Assembly Program and the corresponding nephanalyses which were derived from the satellite videographs. These analyses are shown in figures 10 through 13 and will be briefly discussed.

The layer-cloudiness nephanalysis based on TIROS IX pass 0137 (1530 GMT, February 2) is shown in figure 10a. The probability-of-cloudiness analysis for 1500 GMT, February 2 and for the corresponding region is shown in figure 10b. In general, an excellent correspondence is in evidence between these two analyses. The frontal band which extended south from Greenland is in juxtaposition with a similarly oriented band in the probability-of-cloudiness distribution. Other regions of correspondence can also be noted: In the cloudiness areas southwest of Ireland, along  $5^{\circ}$  N. latitude, in the cloud-free areas between Ocean Stations D and E, and throughout a broad area over the southeastern North Atlantic Ocean. Discrepancies between the analyses are confined primarily to two areas: south of Iceland and west of the Iberian Peninsula. Re-examination of the original videographs revealed that the clouds south of Iceland (which were in twilight) had an appearance which was suggestive of stratocumulus; it is believed that the discrepancy noted in this area was the result of the incorrect identification of the clouds as being synoptically significant, layer cloudiness. (This type of discrepancy will hereafter be denoted as a Category I discrepancy.) In the area to the west of the Iberian Peninsula, the discrepancy is attributed to an incorrect mass-structure analysis. In order to produce a probability-of-cloudiness of nine-tenths or greater, it would have been necessary for the parcels to have experienced net lifting during their prior trajectories; as the satellite observations showed this area to have been cloud-free, the diagnosed lifting in this area must have been excessive. This indicates that the phase relationship between the stream function and the pressure-height contours of the isentropic surface in this area was in error and/or the gradients of these fields were inaccurate. (Errors from this source will hereafter be denoted as Category II discrepancies.)

The nephanalysis based on pass 0138 (1730 GMT, February 2) is shown in figure 11a; the corresponding probability-of-cloudiness analysis is shown in figure 11b. The correspondence between these two fields again is fairly good. The frontal band off the east coast of the United States has been diagnosed in the probability-of-cloudiness analysis (although it is much broader in the latter analysis); the trailing portion of the frontal band along  $30^{\circ}$  N. latitude and the band of cloudiness along  $5^{\circ}$  N. latitude are reflected with reasonable accuracy in the probability-of-cloudiness analysis. Several areas

of disagreement are also evident; these are: southeast of Newfoundland, in the southwestern Atlantic near  $17.5^{\circ}$  N.,  $52^{\circ}$  W., and over the Caribbean Sea. The discrepancy in the first area falls under Category I while the remainder are Category II type discrepancies.

In figure 12a is shown the nephanalysis based on TIROS IX pass 0140 (2130 GMT), with the corresponding probability-of-cloudiness analysis for 2100 GMT, February 2 in figure 12b. With the exception of northern Mexico, the diagnosed probability-of-cloudiness distribution over the land areas was in excellent agreement with the observed cloudiness. The discrepancy noted over northern Mexico is in Category II although surface heating effects may also have been a contributing factor. Surprisingly, there is also agreement in the Baja California area and to the west and southwest of this peninsula; this suggests that the mass-structure analysis over this area was reasonably accurate. South of Mexico, over the tropical Pacific Ocean, the probability-of-cloudiness analysis is completely erroneous. The agreement in the remainder of the eastern Pacific was generally poor. Near  $25^{\circ}$  N.,  $130^{\circ}$  W., a frontal band was present in the observed cloudiness; a suggestion of this system was evident in the probability-of-cloudiness analyses, but correspondence between the two systems was not particularly good. In addition, the detail present in the nephanalysis was almost entirely lacking in the probability-of-cloudiness analysis. These discrepancies are attributed entirely to the lack of information in the mass-structure analysis (particularly in the smaller wavelength features) over the eastern Pacific Ocean.

The last comparison of this experiment is shown in figure 13. The nephanalysis based on TIROS IX pass 0141 (2330 GMT) is shown in figure 13a and the probability-of-cloudiness analysis for 0000 GMT, February 3 in figure 13b. The dependence of the accuracy of the probability-of-cloudiness analysis on the information content of the mass-structure analyses is clearly illustrated by this figure. The pattern of the probability-of-cloudiness analysis shows a very general correspondence with the observed cloudiness but there is a complete lack of detail in the prior analysis. This is particularly evident in the area to the north of the Hawaiian Islands where no upper-air data are available.

## 6. DISCUSSION OF RESULTS

An assembly program to assimilate information derived from satellite videographs and produce a probability-of-cloudiness analysis for times concurrent with the standard, synoptic, upper-air observations has been formulated, programed, and tested.

The results of Experiments No. 1 and No. 2 indicate that the accuracy of the probability-of-cloudiness analyses depends more on the accuracy of the diagnosed, net lifting of the parcels than on the constants contained in the formulation of the Program. This fact is inherent in the pressure-dependent, significant-threshold, mixing-ratio

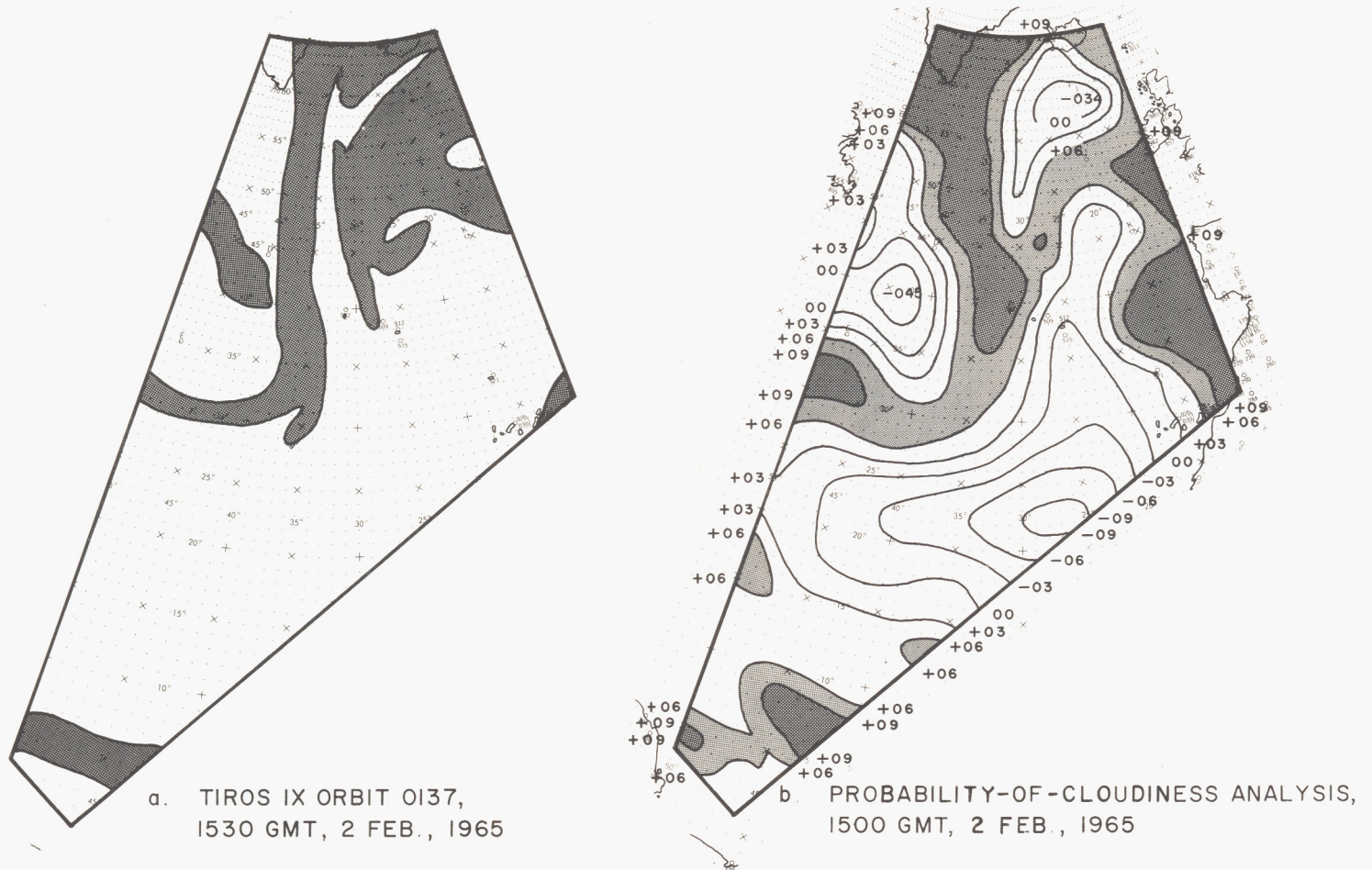


FIGURE 10.—Experiment No. 4: comparison between the probability-of-cloudiness analysis produced without cloud input for 1500 GMT, February 2, 1965 and the observed conditions of cloudiness. (For legend see fig. 4.)

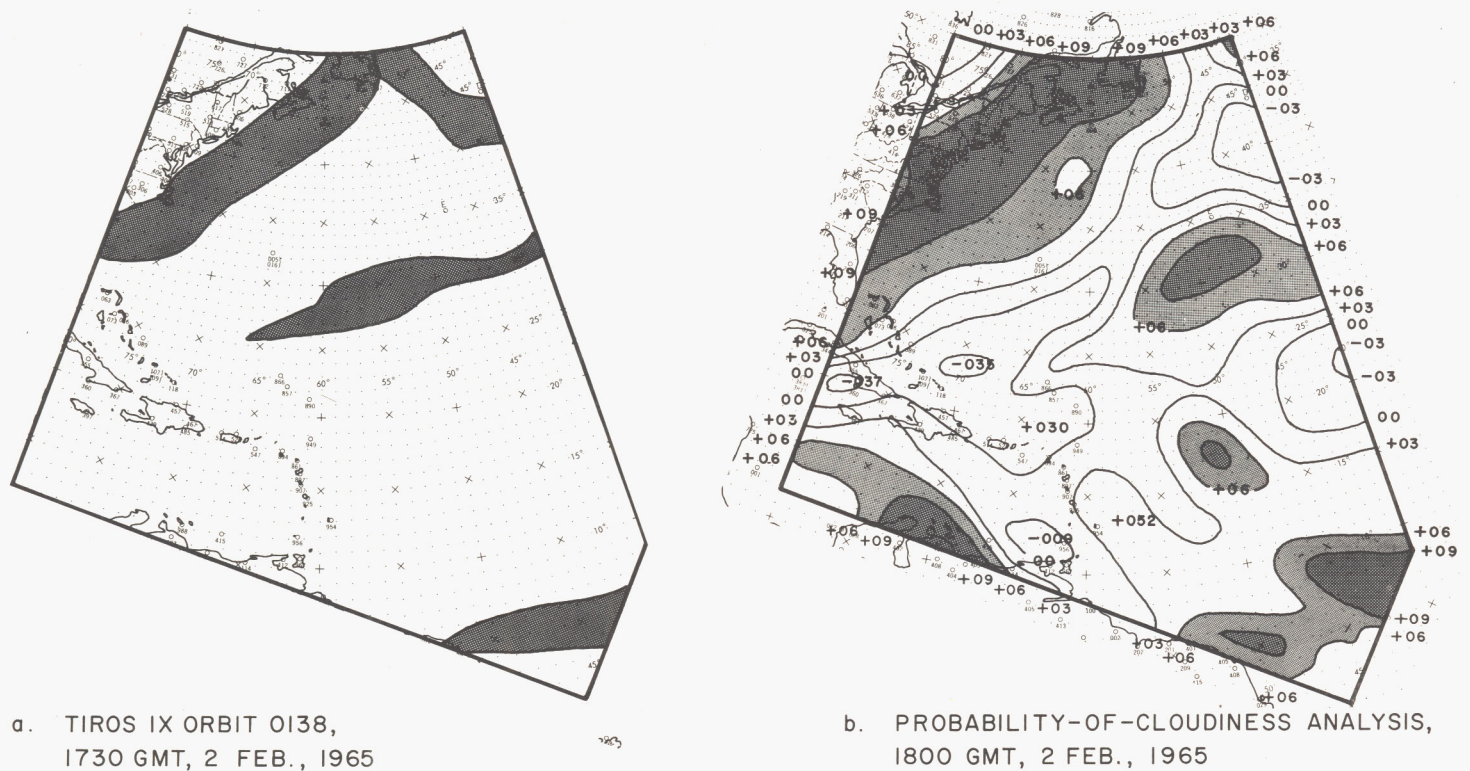
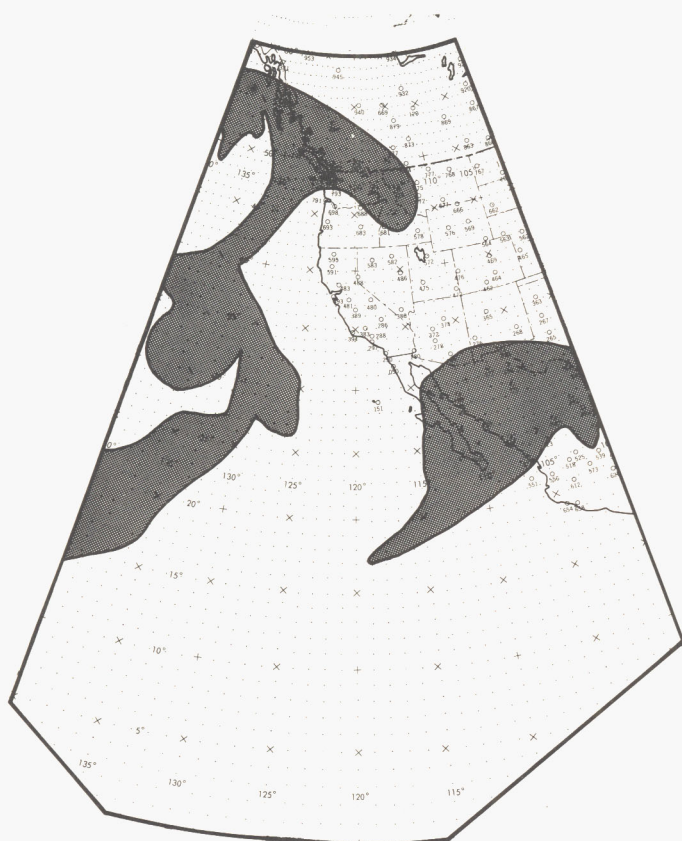


FIGURE 11.—Experiment No. 4: comparison between the probability-of-cloudiness analysis produced without cloud input for 1800 GMT, February 2, 1965 and the observed cloudiness. (For legend see fig. 4.)





a. TIROS IX ORBIT 0140,  
2130 GMT, 2 FEB., 1965

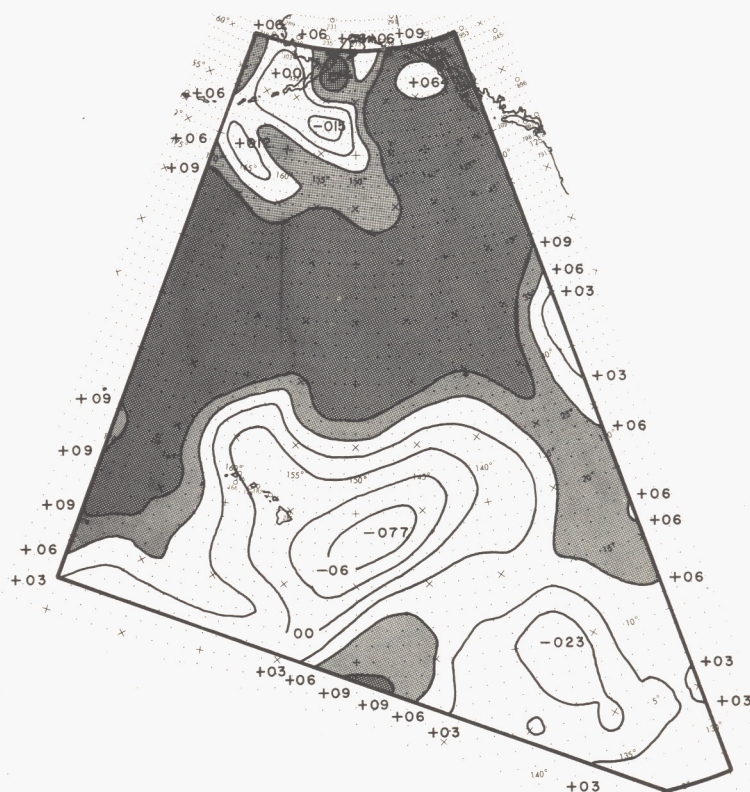


b. PROBABILITY-OF-CLOUDINESS ANALYSIS,  
2100 GMT, 2 FEB., 1965

FIGURE 12.—Experiment No. 4: comparison between the probability-of-cloudiness analysis produced without cloud input for 2100 GMT, February 2, 1965 and the observed cloudiness. (For legend see fig. 4.)



a. TIROS IX ORBIT 0141,  
2330 GMT, 2 FEB., 1965



b. PROBABILITY-OF-CLOUDINESS ANALYSIS,  
0000 GMT, 3 FEB., 1965

FIGURE 13.—Experiment No. 4: comparison of the probability-of-cloudiness analysis produced without cloud input for 0000 GMT, February 3, 1965 with the observed cloudiness. (For legend see fig. 4.)

TABLE 1.—*Subsidence required for a fully cloudy parcel to reach the zero-cloudiness threshold*

$p_a$ (mb.)	$\Delta p_a$ (mb.)
100	+270
200	+178
300	+107
400	+076
500	+068
600	+068
700	+066
800	+052
900	+038
1000	+020

curves shown in figure A1 of the Appendix. On the basis of the data from which the curves of figure A1 were derived and on the assumption that the combined mixing ratio is parcel conservative (except for the upper bound,  $W_m$ , maintained by precipitation), the effect on cloud amount in ascending and descending air parcels can be estimated from these curves. For a fully cloudy parcel at pressure  $p_a$  the parcel must descend to some pressure  $p_b$  for the water substance in cloud form to completely evaporate; selected values of  $p_a$  and the corresponding subsidence required to reach the zero-cloudiness threshold are provided in table 1.

It is apparent from table 1 that cloudiness responds much more rapidly to vertical motions at low levels (higher pressures) than at high levels (lower pressures). This characteristic is borne out by the known persistence of high-level cirrus. The physical reason for this is that air parcels with very low temperatures have very little capacity to hold moisture in *vapor form*; these air parcels must, therefore, undergo considerable descent before the temperature of the parcel is raised sufficiently to hold the water substance suspended in the cloud droplet or ice crystals.

Table 1 also indicates that, except for extremely dry air parcels, a relatively small amount of lifting is required to generate cloudiness in the low and middle portions of the troposphere. As shown in our previous studies (see e.g., Nagle and Clark [4]), the net lifting or subsidence of parcels in selected regions of middle-latitude cyclones can exceed 10 mb. per hr. Such high rates can be sustained for 24 hr. or more. In such regions, it is apparent from table 1 that the net lifting or subsidence is more than sufficient to form new cloudiness or dissipate existing cloudiness. Therefore, in regard to the generation or dissipation of layer-cloudiness, the initial moisture content of a parcel is relatively unimportant in comparison to the net lifting or subsidence the parcel experienced during its prior history. As the accuracy of the diagnosed net horizontal and vertical displacement of the parcels is primarily dependent on the accuracy of the mass-structure analyses, the accuracy of the resultant probability-of-cloudiness analyses is highly dependent on the accuracy of the mass-structure analyses.

The results of Experiments No. 1 and No. 2 have shown that in regions where the mass-structure analysis is in-

correct, very little of the information contained in the assimilated cloud data will be retained in the resultant probability-of-cloudiness analysis over periods of 12 or 24 hr. In contrast, and as shown by the results of Experiments No. 4, in regions of relatively dense data coverage, the probability-of-cloudiness analyses produced without the assimilation of cloud information compared favorably with the observed cloudiness patterns. On the basis of these results, there appears to be little justification for assimilating the cloud information into the Cloud Assembly Program.

In conclusion, it is believed that the Cloud Assembly Program modified to allow integration without the assimilation of cloud data would be a highly useful addition to a numerical weather analysis system. It would provide the product-users with numerically produced fields in terms of weather parameters, i.e., the probability of significant layer-cloudiness and accumulated precipitation; these products could also be usefully applied in numerical programs involving computations of the interaction of the hydrometeors in other physical processes such as atmospheric heat-budget and air-sea interaction programs. In addition, the mixing-ratio field (which is available from the Cloud Assembly Program) provides a Northern Hemisphere moisture analysis which is compatible with the evolving mass-structure distribution. By cycling the Program at several different isentropic levels, it would be possible to generate a three-dimensional moisture distribution which could be used in moist numerical prediction models. Lastly, the probability-of-cloudiness analyses would provide information both in the interpretation of satellite videographs and on where the mass-structure analyses should be corrected on the basis of satellite cloud information. In this context, it is interesting to note that, although the smaller-scale details were lacking, the large-scale pattern of the probability-of-cloudiness analyses did show considerable realism even in sparse-data regions. As could be expected, this implies that the accuracy of the objective mass-structure analysis is higher for the long wavelength features than for the shorter wavelength systems. This further suggests that information derived from satellite cloud observation could be most usefully applied in modifying the mass-structure analyses on the scale of the short wavelength troughs and ridges.

## APPENDIX

### SPECIFICATION OF THE HYDROMETEOR VERSUS MIXING RATIO RELATIONSHIPS

For present purposes we add the mixing ratio for water vapor,  $W_v$ , and the mixing ratio for cloud droplets,  $W_l$ , to form the combined mixing ratio for a parcel:

$$W = W_v + W_l \quad (A1)$$

The mixing ratio is defined as the water mass divided by the dry-air mass.

The maximum value of the combined mixing ratio is attained by an air parcel which is vapor saturated and fully cloudy:

$$W_m = W_{vm} + W_{lm}. \quad (A2)$$

The vapor portion,  $W_{vm}$ , can readily be estimated on the basis of 100 percent relative humidity; the estimation of the droplet portion rests on limited observations and speculations regarding average conditions.

The saturation vapor mixing ratio is calculated in the order of the steps shown in table A1. Values are shown for the sampling of pressure levels indicated in column (1). Since we are dealing with an isentropic distribution, of selected potential temperature

$$\theta = 305^\circ \text{ K.}, \quad (A3)$$

the temperatures, given in column (2), are obtained from

$$T = [p/1000]^{R/c_p} \cdot \theta. \quad (A4)$$

The saturation vapor-pressure values, given in column (3) as  $e_s$ , are obtained for these temperatures from standard tables [7]. These values are transformed into the saturation mixing ratio according to the formula

$$W_s = \frac{\epsilon e_s}{p - e_s}, \quad (A5)$$

where  $\epsilon = 0.62197$ . The values are given in column (4).

Davis [8] cites average values for water content representative of layer-type cloudiness. His values, based on referenced sources, are reproduced in column (5) of table A1. In order to convert these to mixing ratio we require the dry-air density,  $\rho_a$ , at these pressures, for a parcel with the selected potential temperature of  $305^\circ \text{ K}$ . The densities, given in column (6), are calculated from

$$\rho_a = p[RT]^{-1}, \quad (A6)$$

where  $R$  is the gas constant for dry air, and the temperatures are taken from column (2). The fully cloudy droplet mixing ratios, given by

$$W_{lm} = \rho_l / \rho_a, \quad (A7)$$

are given in column (7). The combined maximum values, column (4) plus column (7), are given in column (8).

The effective mixing ratio,  $W_i$ —with which we associate zero cloudiness but beyond which we associate linear cloud increase—is estimated indirectly. We first estimate mixing ratios associated with a five-tenths cloud cover:

$$W_c = W_{vc} + W_{lc}. \quad (A8)$$

For the liquid content we reduce the fully cloudy values, column (7), to about 30 percent cloud filled on the basis of the available statistics [8]. Some smoothing is introduced in fitting the entire structure. The values are given in column (9). For the vapor content we assume a relative humidity function,

$$r_c = 0.60 + 0.35[p/1000]^2 \quad (A9)$$

This function is a representative fit of differing values given by Smagorinsky [9], Davis [8], and Edson [10]. The indicated values are given in column (10). The corresponding vapor mixing ratios, given in column (11), are obtained from

$$W_{vc} = \frac{\epsilon r_c e_s}{p - r_c e_s} \quad (A10)$$

The combined mixing ratio, associated with five-tenths cloud cover, is given in column (12).

The effective mixing ratio,  $W_i$ , defined earlier, is calculated on the assumption that  $W_c$  is associated with  $\delta_c = 0.3$ , that is, five-tenths of cloud cover relates to about 30 percent of the volume being filled with cloud. On this basis, and further assuming a linear relationship between portions of the volume filled with cloud,  $\delta$ , and combined mixing ratio,  $W$ , we obtain

$$W_i = W_m - \frac{1.0}{0.7} [W_m - W_c] \quad (A11)$$

The resulting values are given in column (13).

Although only selected pressures in the range 450–850 mb. are included in table A1 we have made the estimations (including extrapolations) and calculations in detail for the full range of pressure. The resulting curves for  $W_i$  and  $W_m$ , as functions of pressure, are given in figure

TABLE A1.—Pressure-dependent functional values of mixing ratio for  $\Theta = 305^\circ \text{ K}$ .

(1)	(2)	(3)	(4)	(5)	(6)	(7)	(8)	(9)	(10)	(11)	(12)	(13)
$p$ (mb.)	$T$ ( $^\circ\text{C}$ .)	$e_s$ (mb.)	$W_s = W_{vm}$	$\rho_l$ (gm. m. $^{-3}$ )	$\rho_a$ (gm. m. $^{-3}$ )	$W_{lm}$	$W_m$	$W_{lc}$	$r_c$	$W_{vc}$	$W_c$	$W_i$
450	−30.4	0.4899	0.000678	0.10	645.8	0.000155	0.000833	0.000035	0.67	0.000454	0.000489	0.000342
500	−23.0	0.9649	.001202	.11	696.3	.000158	.001360	.000038	.69	.000829	.000867	.000656
550	−16.1	1.7451	.001980	.14	745.4	.000188	.002168	.000042	.71	.001404	.001446	.001137
600	−9.6	2.9544	.003078	.18	793.1	.000227	.003305	.000049	.73	.002244	.002293	.001859
650	−3.5	4.7187	.004548	.24	839.8	.000286	.004834	.000060	.75	.003405	.003465	.002878
700	2.3	7.2074	.006471	.36	885.4	.000407	.006878	.000081	.77	.004970	.005051	.004268
750	7.8	10.577	.008897	.50	930.0	.000538	.009435	.000119	.80	.007097	.007216	.006265
800	13.0	14.969	.01186	.53	974.0	.000544	.012404	.000127	.82	.009692	.009819	.008710
850	18.0	20.630	.01547	.30	1017.0	.000383	.015853	.000115	.85	.01310	.013215	.012084



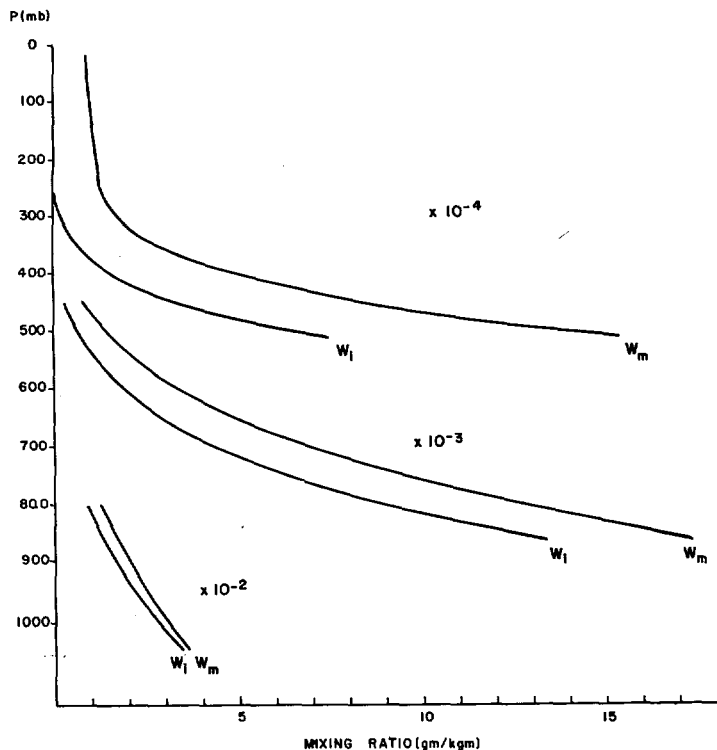


FIGURE A1.—Pressure variability of the significant threshold mixing ratio for  $\theta = 305^\circ \text{ K}$ .

A1. In order to reveal these functions graphically the curves are shown in three sectors scaled as indicated.

The combined mixing ratio curves we have arrived at—the significant values,  $W_i$  and  $W_m$ —are empirical functions designed for the workings of the assembly-and-integration program. In this context the vertical variation and the dynamic range,  $W_m - W_i$ , are significant; the absolute values are not critical.

## REFERENCES

1. R. E. Nagle, J. R. Clark, and M. M. Holl, "Tests of the Diagnostic-Cycle Routine in the Interpretation of Layer-Cloud Evolutions," *Monthly Weather Review*, vol. 94, No. 2, Feb. 1966, pp. 55-66.
2. R. E. Nagle, J. R. Clark, and M. M. Holl, "Evaluation of the Diagnostic-Cycle Routine in the Interpretation of Layer-Cloud Evolutions," *Final Report*, Contract No. Cwb-10884, Meteorology International Inc., Monterey, Calif., 1965, 87 pp.
3. M. M. Holl, J. P. Bibbo, and J. R. Clark, "Linear Transforms for State-Parameter Structure," *Technical Memorandum No. 1*, Ed. 2, Contract N228-(62271)58264, Meteorology International Inc., Monterey, Calif., 1963, 29 pp.
4. R. E. Nagle and J. R. Clark, "Interpretive Uses of the Diagnostic-Cycle Routine," *Final Report*, Contract No. Cwb-11254, Meteorology International Inc., Monterey, Calif., 1966.
5. G. 'Arnason, "A Convergent Method for Solving the Balance Equation," *Journal of Meteorology*, vol. 15, No. 2, Apr. 1958, pp. 220-225.
6. G. 'Arnason and M. Reese, "The Balance Equation Solved Numerically by a Cyclic Procedure," *Internal Technical Report*, U.S. Fleet Numerical Weather Facility, Monterey, Calif., 1961.
7. *Smithsonian Meteorological Tables*, Sixth Revised Ed., Smithsonian Institution, Washington, D.C., 1958.
8. P. Davis, "The Incorporation of Physical Parameters in the Objective Specification of Cloudiness," *Final Report*, Contract AF 19(604)-7343, Stanford Research Institute, Menlo Park, Calif., 1962.
9. J. Smagorinsky, "On the Dynamical Prediction of Large-Scale Condensation by Numerical Methods," pp. 71-78 in "Physics of Precipitation," *Geophysical Monograph No. 5*, American Geophysical Union, Washington, D.C., 1960.
10. H. Edson, "Numerical Cloud and Icing Forecasts," *Scientific Services Technical Note 13*, Headquarters, 3d Weather Wing, Air Weather Service, 1965.

[Received November 21, 1966; revised February 1, 1967]